


## Ultra-high photoresponsive photodetector based on $ReS_2/SnS_2$ heterostructure

Binghui Wang(王冰辉), Yanhui Xing(邢艳辉), Shengyuan Dong(董晟园), Jiahao Li(李嘉豪), Jun Han(韩军), Huayao Tu(涂华垚), Ting Lei(雷挺), Wenxin He(贺雯馨), Baoshun Zhang(张宝顺), and Zhongming Zeng(曾中明)
**Citation:**Chin. Phys. B, 2023, 32 (**9**): 098504. DOI: 10.1088/1674-1056/acd9c0
Journal homepage: http://cpb.iphy.ac.cn; http://iopscience.iop.org/cpb

**What follows is a list of articles you may be interested in**

---

## A field-effect $WSe_2$/Si heterojunction diode

Rui Yu(余睿), Zhe Sheng(盛喆), Wennan Hu(胡文楠), Yue Wang(王越), Jianguo Dong(董建国), Haoran Sun(孙浩然), Zengguang Cheng(程增光), and Zengxing Zhang(张增星)
Chin. Phys. B, 2023, 32 (**1**): 018505. DOI: 10.1088/1674-1056/ac9049

## Graphene-based heterojunction for enhanced photodetectors

Haiting Yao(姚海婷), Xin Guo(郭鑫), Aida Bao(鲍爱达), Haiyang Mao(毛海央),Youchun Ma(马游春), and Xuechao Li(李学超)
Chin. Phys. B, 2022, 31 (**3**): 038501. DOI: 10.1088/1674-1056/ac1b8b

## A double quantum dot defined by top gates in a single crystalline InSb nanosheet

Yuanjie Chen(陈元杰), Shaoyun Huang(黄少云), Jingwei Mu(慕经纬), Dong Pan(潘东), Jianhua Zhao(赵建华), and Hong-Qi Xu(徐洪起)
Chin. Phys. B, 2021, 30 (**12**): 128501. DOI: 10.1088/1674-1056/abff2e

## Effect of electrical contact on performance of $WSe_2$ field effect transistors

Yi-Di Pang(庞奕荻), En-Xiu Wu(武恩秀), Zhi-Hao Xu(徐志昊), Xiao-Dong Hu(胡晓东), Sen Wu(吴森), Lin-Yan Xu(徐临燕), and Jing Liu(刘晶)
Chin. Phys. B, 2021, 30 (**6**): 068501. DOI: 10.1088/1674-1056/abd752

## Field-effect transistors based on two-dimensional materials for logic applications

Wang Xin-Ran (王欣然), Shi Yi (施毅), Zhang Rong (张荣)
Chin. Phys. B, 2013, 22 (**9**): 098505. DOI: 10.1088/1674-1056/22/9/098505

---

# Ultra-high photoresponsive photodetector based on $ReS_2/SnS_2$ heterostructure

Binghui Wang(王冰辉)[1,2], Yanhui Xing(邢艳辉)[1,†], Shengyuan Dong(董晟园)[1], Jiahao Li(李嘉豪)[1], Jun Han(韩军)[1], Huayao Tu(涂华垚)[2], Ting Lei(雷挺)[2], Wenxin He(贺雯馨)[1], Baoshun Zhang(张宝顺)[2], and Zhongming Zeng(曾中明)[2,‡]

[1] *Key Laboratory of Opto-electronics Technology, Ministry of Education, College of Microelectronics, Beijing University of Technology, Beijing* 100124, *China*

[2] *Nanofabrication Facility, Suzhou Institute of Nano-Tech and Nano-Bionics, Chinese Academy of Sciences, Suzhou* 215123, *China*

(Received 23 January 2023; revised manuscript received 13 May 2023; accepted manuscript online 30 May 2023)

Photodetectors based on two-dimensional materials have attracted much attention because of their unique structure and outstanding performance. The response speed of single $ReS_2$ photodetector is slow exceptionally, the heterostructure could improves the response speed of $ReS_2$-based photodetector, but the photodetectors responsivity is reduced greatly, which restricts the development of $ReS_2$. In this paper, a vertically structured $ReS_2/SnS_2$ van der Waals heterostructure photodetectors is prepared, using $ReS_2$ as the transport layer and $SnS_2$ as the light absorbing layer to regulate the channel current. The device has an ultra-high photoconductive gain of $10^{10}$, which exhibits an ultra-high responsivity of 4706 A/W under 365-nm illumination and response speed in seconds, and has an ultra-high external quantum efficiency of $1.602\times10^6$% and a high detectivity of $5.29\times10^{12}$ jones. The study for $ReS_2$-based photodetector displays great potential for developing future optoelectronic devices.

**Keywords:** two-dimensional material, $ReS_2$, heterostructure, photodetector

**PACS:** 85.60.–q, 85.60.Gz, 73.40.Lq **DOI:** 10.1088/1674-1056/acd9c0

## 1. Introduction

Transition metal dichalcogenides (TMDs) with the chemical formula $MX_2$ ($X$ = S, Se, Te and $M$ = transition metal) are widely used in various fields due to their weak interlayer coupling, good optical transparency, and large bandgap,[1–3] such as gas sensors,[1] photodetectors,[4] inverters, and solar cells. Most of the previous researches on TMDs have focused on the Mo and W families, which summarized the material growth and device preparation of photodiodes and rectifiers.[5–9] However, the recently discovered $ReS_2$ possesses properties quite different from $MoS_2$, which has aroused extensive researches.[10,11] First, due to the twisted 1T crystal structure of $ReS_2$, it has a direct bandgap independent of thickness,[12,13] which makes the optical properties of bulk $ReS_2$ and single-layer $ReS_2$ similar, provides a good basis for mechanical exfoliation. In addition, $ReS_2$ has an ultra-high light absorption rate. It has been reported in the literature that the responsivity of multilayer $ReS_2$ photodetectors can reach 88600 A/W.[14] However, one of the most serious problems of $ReS_2$ photodetectors is the slow response speed, which reaches hundreds of seconds.[15] In order to solve this problem, researchers have adopted heterostructures. Two-dimensional heterojunctions materials are combined by van der Waals forces and not affected by lattice mismatch, and different materials can be freely matched, and the detectors with heterojunctions can exhibit various interesting properties.[15,16] For example, the $ReS_2$/graphene/$WSe_2$ heterojunction photodetector prepared by Wang *et al.* has a response speed of 44 ms under 532-nm light.[17] The $ReS_2/ReSe_2$ heterojunction photodetector prepared by Cho *et al.* has a similar response time of 0.4 s under 400-nm and 550-nm light.[12] Although the response speed of the devices was been greatly improved, it is at the expense of the responsivity. The device responsivity of Wang *et al.*[17] is 430 mA/W, and that of Cho *et al.*[12] is only 21.07 mA/W.

In this paper, it is reported that the photodetector based on $ReS_2$ has ultra-high responsivity and response speed in seconds. We chose $SnS_2$ material as the light absorbing layer, and prepared a vertical structure $ReS_2/SnS_2$ heterojunction photodetector. The detector has a responsivity of 4706 A/W under 365-nm light, which is higher than the previously reported detectors based on $ReS_2$ heterojunction,[15,18] and the response speed of the detector is only 1.4 seconds. In addition, our detector also had a high detectivity of $5.29\times10^{12}$ Jones and an ultra-high external quantum efficiency (EQE) of $1.602\times10^6$%. The study paved the way for improving responsivity and reducing response time of the $ReS_2$-based heterostructures photodetector.

†Corresponding author. E-mail: xingyanhui@bjut.edu.cn
‡Corresponding author. E-mail: zmzeng2012@sinano.ac.cn

© 2023 Chinese Physical Society and IOP Publishing Ltd 

## 2. Experimental details

### 2.1. Device fabrication

The $ReS_2/SnS_2$ heterostructure device was fabricated on the $SiO_2$/Si substrate using a dry transfer technique. The few-layer flakes of $ReS_2$ and $SnS_2$ were mechanically exfoliated from commercially bulk crystal. First, the thin $ReS_2$ flakes were exfoliated on a highly p-doped Si substrate with a 300-nm-thick $SiO_2$ layer. Then, the same method was adopted for transferring several layers $SnS_2$ onto the $ReS_2$ under the optical microscope assisted by aligned transfer system. Finally, to fabricate the heterostructure device, the electrode patterns were produced by electron–beam lithography system (EBL, Raith eLINE Plus) and Ti/Au (10 nm/50 nm) metals were deposited by electron–beam evaporation (Ulvac Ei-5z) to form source and drain electrodes.

### 2.2. Result and discussion

Figure 1(a) shows the schematic diagram of the $ReS_2$/$SnS_2$ heterojunction device. The mechanical exfoliation $ReS_2$ and $SnS_2$ were transferred to an $SiO_2$/Si substrate sequentially. The electrodes are placed on the $ReS_2$. In order to obtain the interface information of $ReS_2$ and $SnS_2$ layer of the device, the high-resolution transmission electron microscope (HRTEM) was used, as shown in Fig. 1(b). The interfaces between $SnS_2$ and $ReS_2$, $ReS_2$ and substrate are clear and flat. Figure 1(c) shows the energy dispersive x-ray spectroscopy (EDS) of the device. The distribution of each layer element was uniform, and these elements are corresponding to each layer material of HRTEM, indicating that no diffusion and impurity element were introduced in the process of device preparation. The thickness of $ReS_2$ (8 nm) and $SnS_2$ (14 nm) is shown by atomic force microscopy (AFM) in Fig. 1(d), and the inset is the surface topography image of the heterojunction. Figure 1(e) is the Raman spectrum of the single $ReS_2$ and $SnS_2$ material and the $ReS_2/SnS_2$ heterojunction. $SnS_2$ (the blue line) has a main peak $A_{1g}$ at 313.4 $cm^{-1}$, which is consistent with the literature report.[19] Typical Raman characteristic peaks of $ReS_2$ (the red line) are also observed at 154 $cm^{-1}$ ($E_{2g}$) and 215 $cm^{-1}$ ($A_{1g}$).[20] The black line in Fig. 1(e) shows the characteristic peaks of the $ReS_2/SnS_2$ heterojunction. The above peaks are observed in overlapping areas, indicating the good quality of the heterojunction. Figure 1(f) is the scanning electron microscope image of the device after the preparation of the electrodes. The light absorption layer $SnS_2$ and the transmission layer $ReS_2$ could be clearly observed, and the electrodes are only connected on the $ReS_2$, and the device is regular in shape and a clean surface. The above results show the good structure and successful fabrication of the $ReS_2/SnS_2$ heterojunction device.

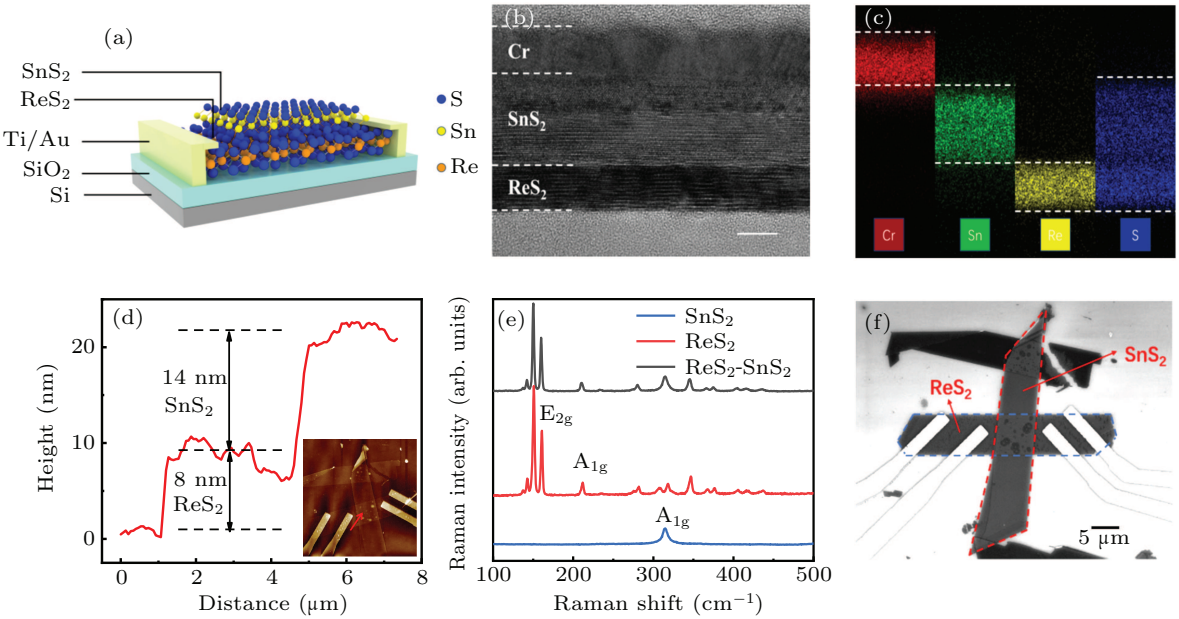



**Fig. 1.** Characterization of $ReS_2/SnS_2$ heterostructure. (a) Schematic diagram of the $ReS_2/SnS_2$ heterostructure. (b) HRTEM image. Scale bar: 10 μm. (c) EDS of the corresponding elements of the photodetector. (d) Height profiles of corresponding $ReS_2$ and $SnS_2$ flakes in AFM. The inset shows a topographic AFM image of the $ReS_2/SnS_2$ device. (e) Raman spectrum of the isolated $ReS_2$, isolated $SnS_2$, and their overlapped regions. (f) The SEM image of the heterostructure, where the scale bar is 5 μm.

The transport properties of the device under dark conditions were measured. Figure 2(a) shows the relationship of the source–drain current ($I_{ds}$) and the source–drain voltage ($V_{ds}$) when the gate voltage ($V_g$) varies from −80 V to 80 V. The $I_{ds}$–$V_{ds}$ curves are straight lines passing through the origin, indicating that $ReS_2$ forms a good ohmic contact with Ti/Au. As $V_g$ increases, the current increases accordingly, meaning that the device has obvious gate voltage control characteristic. Figure 2(b) shows the $I_{ds}$–$V_g$ relationship of the device when $V_{ds}$ changes from −3 V to 3 V. When $V_g$ below −30 V ($V_{th}$), $I_{ds}$

approaches 0 A, and when $V_g$ over −30 V, $I_{ds}$ rises gradually. When the $V_g$ is negative, the direction of the external electric field is opposite to that of the built-in electric field. When $V_g < V_{th}$ (−30 V), the external electric field plays a major role, electrons flow from $ReS_2$ to $SnS_2$ and the carrier concentration decreased, resulting in the current approaches 0 A, when $V_g > V_{th}$ (−30 V), the direction of the electric field pointed from $ReS_2$ to $SnS_2$, and electrons entered $ReS_2$ under the action of the electric field, increasing the carrier concentration in the channel, thereby increasing the drain current. The device also switched from the insulating state to the conducting state, showing obvious n-type conductivity. Figure 2(c) shows the logarithmic curves of $I_{ds}$ versus $V_g$, which characterizes the on-off ratio of the device. The on-off ratio reaches $10^4$, indicating that the device has a high current regulation capability.

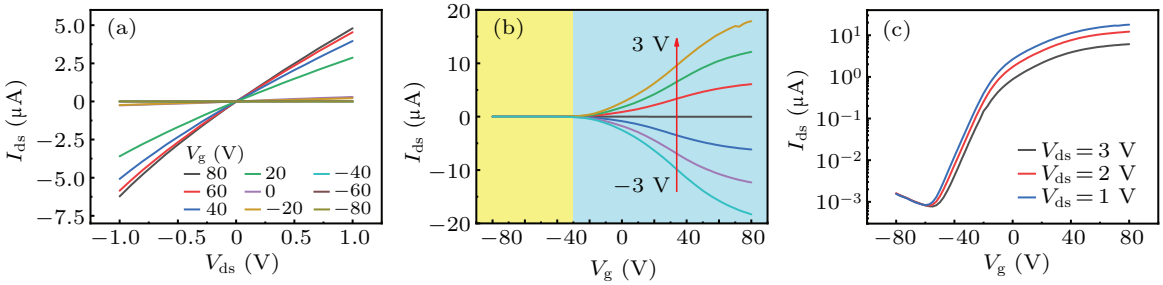



**Fig. 2.** The *I*–*V* characteristics of the device based on $ReS_2/SnS_2$ heterostructure under non-illumination condition. (a) $I_{ds}$–$V_{ds}$ output characteristics under various back gate voltages. (b) $I_{ds}$–$V_g$ transfer curves at various drain voltages. (c) The logarithmic curves of the transfer characteristic curves of the $ReS_2/SnS_2$ heterojunction.

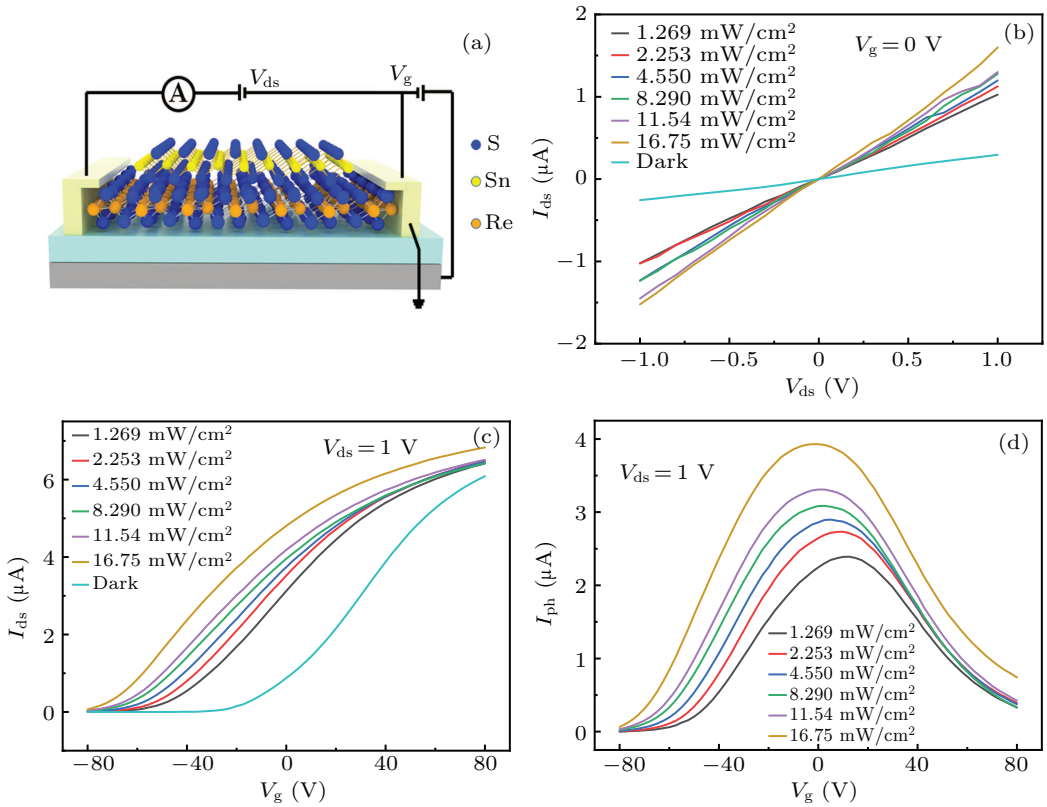



**Fig. 3.** (a) Schematic diagram of the device measure setup. (b) Output characteristic curves under different incident power densities ($V_g$ = 0 V). (c) Transfer characteristic curves of the device under different incident power densities ($V_{ds}$ = 1 V). (d) Photocurrent ($I_{ph}$) as a function of $V_g$ under different incident power densities ($V_{ds}$ = 1 V).

The optoelectrical properties of the device were tested under 365-nm light source. Figure 3(a) is a schematic diagram of the measurement setup, in which the gate voltage is applied on the backside of the heterojunction, and the source–drain voltage is applied on the $ReS_2$. Figure 3(b) shows the output characteristic curves under different incident power intensities when the gate voltage is 0 V. Compared with the $I_{ds}$ under dark conditions, the $I_{ds}$ is significantly improved under illumination. The light absorption layer $SnS_2$ was irradiated, a large number of photogenerated carriers were generated, and transported into $ReS_2$ under the action of the built-in electric field, resulting in increasing the drain current. When $V_{ds}$ is 1 V, the

transfer characteristic curves of the device at different incident power densities are shown in Fig. 3(c). $I_{ds}$ increased with the increase of incident power densities. The gate voltage could effectively regulate the channel current, and a higher gate voltage induced and promoted more carriers to pass through the heterojunction, thereby increasing the photogenerated current. In order to characterize the change of photocurrent with gate voltage more intuitively, we plotted the photocurrent ($I_{ph}$) as a function of $V_g$, as shown in Fig. 3(d). At a certain optical power density and source–drain voltage (1 V), with the increase of the gate voltage, the photocurrent increased first and then decreased, and the peak value of each curve corresponds to a different gate voltage, and the gate voltage shifted to the right with the decrease of the optical power density. Because the photocurrent was modulated by the optical power density and the gate voltage. When the optical power density was high, $SnS_2$ can generate more photogenerated electrons and holes, the concentration of photogenerated electrons in the channel will be greater, so a smaller gate voltage is required to achieve saturation current.

Then, we quantitatively characterized the detection performances of the $ReS_2/SnS_2$ heterojunction at 365 nm, including responsivity ($R$), specific detectivity ($D^*$), EQE, and noise equivalent power (NEP), which could be calculated by the following functions:

$$R = I_{ph}/(P_{in}A), \tag{1}$$

$$D^* = RA^{1/2}/(2eI_{dark})^{1/2}, \tag{2}$$

$$\mathrm{EQE} = hcR\lambda^{-1}e^{-1}, \tag{3}$$

$$\mathrm{NEP} = A^{1/2}/D^*, \tag{4}$$

where $P_{in}$, $A$, $e$, $h$, $c$, and $\lambda$ are the incident optical power density, effective illuminated area, electron charge, Planck's constant, light speed, and incident light wavelength, respectively.

Figure 4(a) shows the gate voltage dependence of responsivity under various incident power densities at $V_{ds} = 1$ V. The responsivity decreased with the increase of the optical power density. When $P_{in} = 1.269$ mW/cm$^2$ and $V_g = 10$ V, the detector reaches the highest responsivity of 4706 A/W, and the responsivity of the detector is much higher than other reported results.[15,18] In addition, the specific detectivity is also an important parameter to evaluate the performance of the detector, which represents the sensitivity of the detector. As shown in Fig. 4(b), when $V_g = 0$ V and $V_{ds} = 1$ V, $D^*$ reduce with the increase of the incident power densities, and the maximum value $5.29\times10^{12}$ Jones is obtained at the minimum incident power densities. Figure 4(c) shows EQE as a function of incident power densities when $V_g = 10$ V and $V_{ds} = 1$ V. EQE reduces with the increase of the optical power density, and the maximum value is $1.602\times10^6$% when $P_{in} = 1.269$ mW/cm$^2$, which shows that our detector has an excellent photoelectric conversion capability. In addition, figure 4(d) shows NEP as a function of the incident power densities when $V_g = 0$ V and $V_{ds} = 1$ V, an ultra-low noise equivalent power of $1.2\times10^{-16}$ W/Hz$^{1/2}$ was obtained when $P_{in} = 1.269$ mW/cm$^2$.

To further illustrate the reason for the high responsivity of the detector, we calculated the photoconductive gain and performed the energy band analysis. The photoconductive gain $G$ is defined as the ratio of minority carrier lifetime $\tau_{life}$ to transit time $\tau_t$, which can be obtained according to the following equations:

$$G = \tau_{life}/\tau_t, \tag{5}$$

$$\tau_t = W^2/\mu V_{ds}, \tag{6}$$

$$\mu = \frac{L}{WC_gV_{ds}}\frac{\mathrm{d}I_{ds}}{\mathrm{d}V_g}, \tag{7}$$

where $W$ and $L$ are the width and length of the detector channel, respectively, and $C_g$ is the capacitance of the gate insulator ($C_{SiO_2} = 1.033\times10^{-8}$ F/cm$^2$). When $V_{ds} = 3$ V, the field-effect mobility $\mu$ and the carrier transport time $\tau_t$ of the device are calculated to be 22.386 cm$^2\cdot$V$^{-1}\cdot$s$^{-1}$ and 0.59 ns, respectively, and the photoconductive gain $G$ is calculated to be about $10^{10}$, which provides a theoretical basis for producing high responsivity. Therefore, the high responsivity of our device is due to the built-in electric field formed by the heterojunction, resulting in an ultra-high photoconductive gain, and the high photoconductive gain allows high responsivity.

Figure 5(a) shows the band arrangement structure of $ReS_2$ and $SnS_2$. The minimum conduction band ($E_c$) and the maximum valence band ($E_v$) of $SnS_2$[21] ($ReS_2$[22]) are $-5.14$ eV ($-4.68$ eV) and $-6.73$ eV ($-6.19$ eV), respectively, which make the $ReS_2/SnS_2$ heterojunction belong to a typical type-II band alignment structure. Electrons transition from $SnS_2$ the valence band to the conduction band under illumination, generating electron–hole pairs. Figure 5(b) is a schematic diagram of carrier transmission under light conditions. Under illumination conditions, photogenerated carriers in $SnS_2$ are collected into $ReS_2$ under the action of the built-in electric field, thus generating a higher photocurrent and greatly improving the photo responsivity of the $ReS_2/SnS_2$ heterojunction. Figure 5(c) shows the dark current of the single $ReS_2$ and the $ReS_2/SnS_2$ heterojunction as a function of the gate voltage. The dark current of the $ReS_2/SnS_2$ heterojunction detector significantly reduced, because the electrons in $ReS_2$ flowed to $SnS_2$ with a low Fermi level under dark conditions, the carrier concentration in $ReS_2$ decreased, thereby reducing the dark current and improving the detectivity of the device for weak light.

Response time is also one of the key parameters to characterize the detector. We compared the optical switching characteristics of the $ReS_2/SnS_2$ heterojunction and a single $ReS_2$

detector under 365-nm light source. The response time refers to the time required for the device to generate photo-generated carriers to change the output current when the photodetector is irradiated. The rising time is defined as the current increase from the 10% to 90% of the saturation current. On the contrary, the falling time indicates the time falling from 90% to 10% of the saturation current when the optical source is removed. The response time of the single $ReS_2$ detector is shown in Fig. 6(a). The rise time is 6.7 s and a fall time of 25.7 s. The long fall response time is attributed to trap states generated in the $ReS_2$ material as a result of its preparation. When $ReS_2$ absorbs photon energy, it generates electron–hole pairs, and a sort of the carriers can become trapped by a trap state, this impedes the recombination of electron–hole pairs in the conductive channel, thereby extending the response time of the $ReS_2$ detector.[14,23,24] The response time of the heterojunction is shown in Fig. 6(b), with a rise time of 1.4 s and a fall time of 7 s. The response speed of the device is obviously improved. It is attributed to the fact that the built-in electric field between $ReS_2$ and $SnS_2$ heterojunction, accelerates the separation of photogenerated electron–hole pairs. Moreover, the device is still stable when the device is optically switched several times. In addition, we also tested the optical switching characteristics of the device under different light source, as shown in Figs. 6(c) and 6(d). The device still has stable optical switching characteristics under 460-nm and 532-nm illuminations.

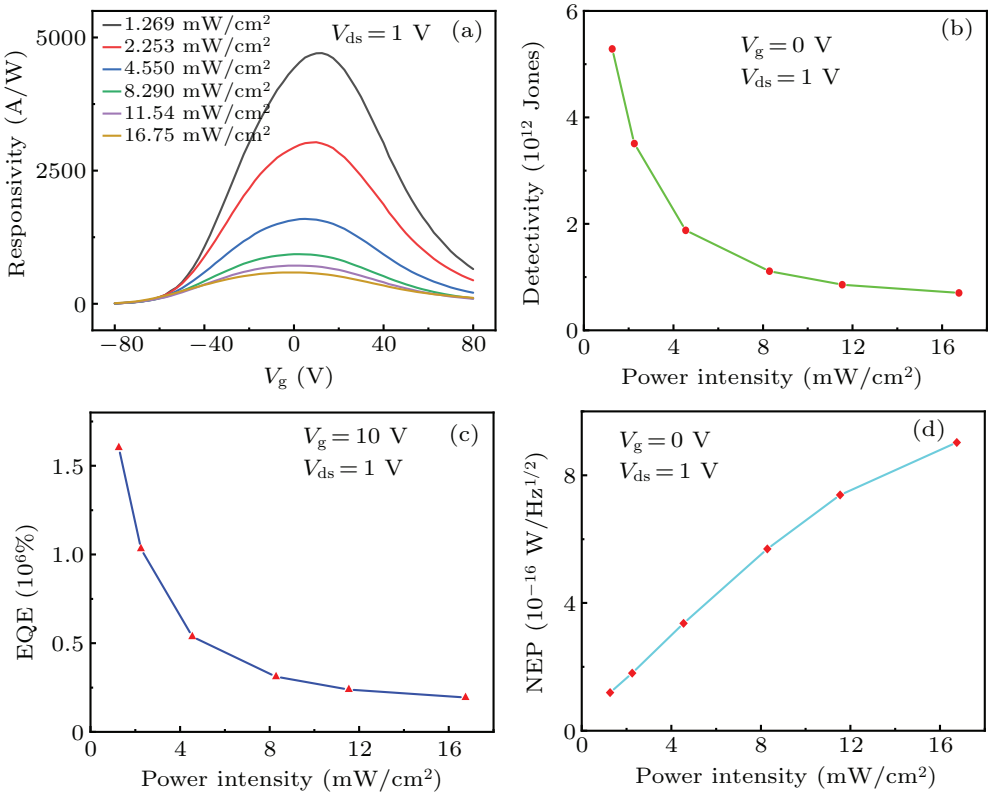



**Fig. 4.** Photoresponse characterizations of the $ReS_2/SnS_2$ photodetector under an illumination wavelength of 365 nm. (a) Responsivity as a function of the applied voltage under various incident power densities ($V_{ds}$ = 1 V ). (b) Detectivity of as a function incident power intensities ($V_g$ = 0 V, $V_{ds}$ = 1 V). (c) The external quantum efficiency (EQE) as a function of incident power intensities ($V_g$ = 10 V, $V_{ds}$ = 1 V). (d) Noise equivalent power (NEP) as a function of incident power intensities ($V_g$ = 0 V, $V_{ds}$ = 1 V).

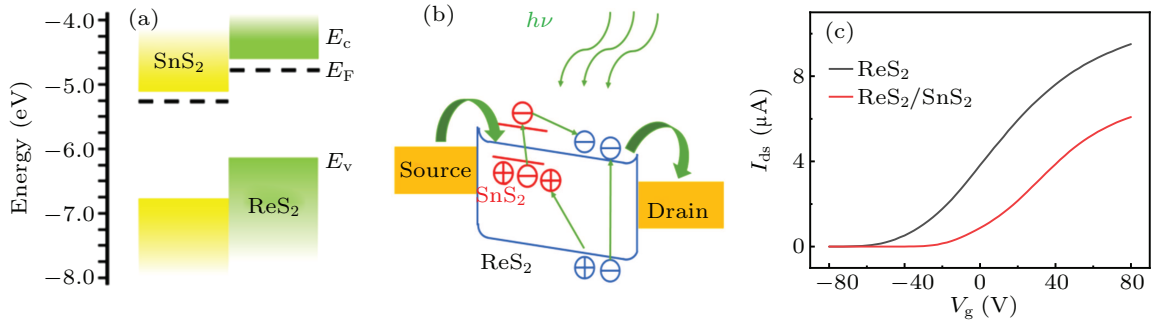



**Fig. 5.** (a) Band structure of $ReS_2/SnS_2$ heterojunction. (b) Schematic diagram of carrier transport of $ReS_2/SnS_2$ heterojunction under illumination. (c) The dark currents of $ReS_2$-based photodetector and $ReS_2/SnS_2$ heterojunction photodetector varying with the gate voltage.

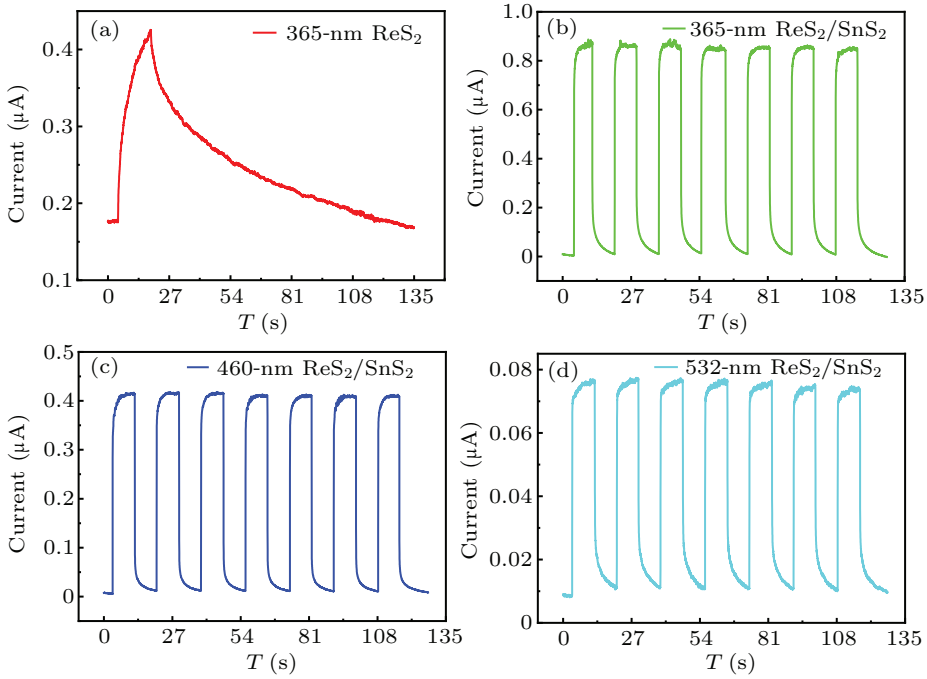



**Fig. 6.** (a) The optical switching characteristic of the $ReS_2$ photodetector at $\lambda = 365$ nm. (b)–(d) The optical switching characteristic of the $ReS_2/SnS_2$ heterostructure photodetector at $\lambda = 365$-nm, 460-nm, and 532-nm wavelengths, respectively.

**Table 1.** Comparison with reported heterojunction photodetectors.

| Device | Laser $\lambda$ (nm) | Responsivity (A/W) | Rise/fall time (ms) | Detectivity (Jones) | Reference |
|---|---|---|---|---|---|
| $ReS_2/SnS_2$ | 365–532 | 4706 | $1.4\times10^{3}$ | $5.29\times10^{12}$ | this work |
| $ReS_2/ReSe_2$ | 400–550 | $21.07\times10^{-3}$ | $0.4\times10^{3}$ | – | [12] |
| $ReS_2$/graphene/$WSe_2$ | 532 | $430\times10^{-3}$ | 44 | – | [17] |
| $MoTe_2/ReS_2$ | 638–1310 | 0.54 | $2.4/3\times10^{-3}$ | $10^{8}$–$10^{9}$ | [22] |
| $Te/ReS_2$ | 632 | 180 | 5 | $10^{9}$ | [25] |
| t-Se/$ReS_2$ | 400 | 98 | 50 | $6\times10^{10}$ | [26] |
| $WSe_2/ReS_2$ | 532 | 3 | $5\times10^{-3}$ | – | [27] |
| Si/ZnO | 254 | $2\times10^{4}$ | $3.97\times10^{3}$ | $6.83\times10^{14}$ | [28] |
| PbS/$MoS_2$ | 780–1100 | $4.5\times10^{4}$ | 7.8 | $3\times10^{13}$ | [29] |

To compare with other heterojunction photodetectors, Table 1 lists the results of other research groups.[12,17,22,25–29] According to the comparison and analysis in the table, although the response speed of the detector is not as fast as other reported results, the responsivity of the detector is much higher than other reported results, and $D^*$ is also about 2–3 orders of magnitude higher than most detectors. In order to improve the responsivity and the response speed of $ReS_2$-based photodetector, the $ReS_2/SnS_2$ heterojunction is a good choice, and it provides a direction for improving the comprehensive performance of the $ReS_2$-based photodetector.

## 3. Conclusion

We have achieved an $ReS_2/SnS_2$ heterojunction photodetector, which presents an ultra-high responsivity of 4706 A/W under 365-nm light irradiation, and the response time is only 1.4 s. In addition, the device also has a high specific detectivity of $5.29\times10^{12}$ Jones, an ultra-high EQE of $1.602\times10^{6}$% and an ultra-low noise equivalent power of $1.2\times10^{-16}$. From the energy band analysis, such a high responsivity is obtained due to the effectively separated electron–hole pairs, which prolongs the lifetime of the carriers, thereby increasing the photocurrent. In conclusion, our $ReS_2/SnS_2$ heterostructures photodetector provides a new way to improve the responsivity of $ReS_2$-based photodetector and shorten the response time of a single $ReS_2$ photodetector.

## Acknowledgements

Project supported by the National Natural Science Foundation of China (Grant Nos. 61574011, 60908012, 61575008, 61775007, 61731019, 61874145, 62074011, and 62134008), the Beijing Natural Science Foundation (Grant Nos. 4182015, 4172011, and 4202010), and Beijing Nova Program (Grant No. Z201100006820096). The authors would like to thank the Nano Fabrication Facility, Vacuum Interconnected Nanotech Workstation at Suzhou Institute of Nano-Tech and Nano-Bionics, Chinese Academy of Sciences, and Laboratory of Nanodevices and Applications, Suzhou Institute of Nano-Tech

and Nano-Bionics, Chinese Academy of Sciences for their technical supports.

## References


[1] Zheng W, Liu X H, Xie J Y, Lu G C and Zhang J 2021 *Coordination Chemistry Reviews* **447** 214151

[2] Gao Z L, Zhao M Q, Ashik M M A and Johnson A T C 2020 *J. Phys. Mater* **3** 042003

[3] Chen G Y, Hu X Y, Gu M W, Wu H, Chen K Y, Yu H, Ren B Y, Li Z, Luan Y G, Tang T, Cheng Y F, Huang H B, Chen L G, Zhang B Y and Ou J Z 2022 *Adv. Funct. Mater.* **32** 2202239

[4] Saha D, Varghese A and Lodha S 2020 *ACS Appl. Nano Mater.* **3** 820

[5] Kang S, Kim Y S, Jeong J H, Kwon J, Kim J H, Jung Y, Kim J C, Kim B, Bae S H, Huang P Y, Hone J C, Jeong H Y, Park J W, Lee C H and Lee G H 2021 *ACS Appl. Mater. Interfaces* **13** 1245

[6] Mortelmans W, Mehta A N, Balaji Y, Kazzi S E, Sergeant S, Houssa M, Gendt S D, Heyns M and Merckling C 2020 *2D Mater* **7** 025027

[7] Zhang X K, Yu H H, Tang W H, Wei X F, Gao L, Hong M Y, Liao Q L, Kang Z, Zhang Z and Zhang Y 2022 *Adv. Mater.* **34** 2109521

[8] Zhang X K, Liu B S, Gao L, Yu H H, Liu X Z, Du J L, Xiao J K, Liu Y H, Gu L, Liao Q L, Kang Z, Zhang Z and Zhang Y 2021 *Nat. Commun.* **12** 1522

[9] Zhang X K, Liao Q L, Kang Z, Liu B S, Ou Y, Du J L, Xiao J K, Gao L, Shan H Y, Luo Y, Fang Z Y, Wang P D, Sun Z, Zhang Z and Zhang Y 2019 *Acs Nano* **13** 3280

[10] Jeon J, Choi H, Baek S, Choi S, Cho J H and Lee S 2021 *Appl. Surf. Sci.* **544** 148865

[11] Moon Y S, Shon J H, Kim D, Lee K, Joo M K and Kim G T 2020 *Appl. Phys. Lett.* **116** 183102

[12] Cho A J, Namgung S D, Kim H and Kwon J Y 2017 *APL Mater.* **5** 076101

[13] Jariwala B, Voiry D, Jindal A, Chalke B A, Bapat R, Thamizhavel A, Chhowalla M, Deshmukh M and Bhattacharya A 2016 *Chem. Mater.* **28** 3352

[14] Liu E F, Long M S, Zeng J W, *et al.* 2016 *Adv. Funct. Mater.* **26** 1938

[15] Ma H X, Xing Y H, Han J, Cui B Y, Lei T, Tu H Y, Guan B L, Zeng Z M, Zhang B S and Lv W M 2022 *Adv. Opt. Mater.* **10** 2101772

[16] Zhang D B, Gao Q, Chen Y Z, Xia Y D, Wang H, Wang H Y and Ni Y X 2020 *Adv. Theory Simul.* **3** 2000144

[17] Wang Z D, Zeng P Y, Hu S J, Wu X M, He J Y, Wu Z T, Wang W H, Zheng P, Zheng H, Zheng L, Huo D X and Zhang Y 2021 *Nanotechnology* **32** 465201

[18] Park S, Ha J, Khan M F, Im C, Park J Y, Yoo S H, Rehman M A, Kang K, Lee S H and Jun S C 2022 *ACS Appl. Electron. Mater.* **4** 4306

[19] Cui B Y, Han J, Xing Y H, Lv W M, Lei T, Ma H X, Zeng Z M and Zhang B S 2021 *Phys. Status Solidi A* **218** 2100228

[20] Xiong Y, Chen H W, Zhang D W and Zhou P 2019 *Phys. Status Solidi RRL* **13** 1800658

[21] Li B, Huang L, Zhong M Z, Li Y, Wang Y, Li J B and Wei Z M 2016 *Adv. Electron. Mater.* **2** 1600298

[22] Ahn J, Kyhm J H, Kang H K, Kwon N, Kim H K, Park S and Hwang D K 2021 *ACS Photon.* **8** 2650

[23] Thakar K, Mukherjee B, Grover S, Kaushik N, Deshmukn M and Lodha S 2018 *ACS Appl. Mater. & Interfaces* **10** 36512

[24] Zhang E, Jin Y B, Yuan X, Wang W Y, Zhang C, Tang L, Liu S S, Zhou P, Hu W D and Xiu F X 2015 *Adv. Funct. Mater.* **25** 4076

[25] Tao J J, Jiang J B, Zhao S N, Zhang Y, Li X X, Fang X S, Wang P, Hu W D, Lee Y H, Lu H L and Zhang D W 2021 *ACS Nano* **15** 3241

[26] Qin J K, Yan H, Qiu G, Si M W, Miao P, Duan Y Q, Shao W Z, Zhen L, Xu C Y and Ye P D D 2019 *Nano Res.* **12** 669

[27] Varghese A, Saha D, Thakar K, Jindal V, Ghosh S, Medhekar N V, Ghosh S and Lodha S 2020 *Nano Lett.* **20** 1707

[28] Yu H H, Liao Q L, Kang Z, Wang Z Y, Liu B S, Zhang X K, Du J L, Ou Y, Hong M Y, Xiao J K, Zhang Z and Zhang Y 2020 *Small* **16** 2005520

[29] Wen Y, Yin L, He P, Wang Z X, Zhang X K, Wang Q S, Shifa T A, Xu K, Wang F M, Zhan X Y, Wang F, Jiang C and He J 2016 *Nano Lett.* **16** 6437